# Platinum-Group Metal Nanoparticles as Peroxidase Mimics: Implications for Biosensing

Alexander Biby,† Harrison Crawford,† Xiaohu Xia†,‡,\*

<sup>†</sup>Department of Chemistry, University of Central Florida, Orlando, Florida 32816, United States

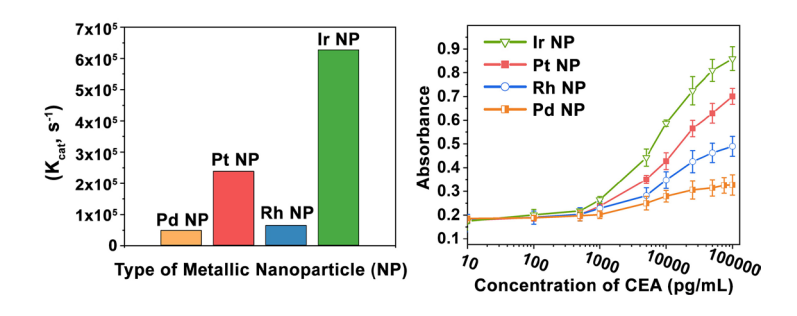
<sup>&</sup>lt;sup>‡</sup>NanoScience Technology Center, University of Central Florida, Orlando, Florida 32816, United States

<sup>\*</sup>Corresponding author. E-mail: Xiaohu.Xia@ucf.edu

#### Abstract

Over the past few decades, peroxidase mimics made of platinum-group metal nanoparticles (PGM NPs) have been actively developed and applied to various biosensing platforms. Nevertheless, there is a lack of comprehensive study that compares the peroxidase-like activities of PGM NPs and their performance in biosensing. Here we report a systematic study of PGM NPs as peroxidase mimics, including Pd, Pt, Rh, and Ir NPs. NPs of these elements were uniformly synthesized and their nanoscale features probed to ensure consistent size, shape, and chemical ligand on the surface. Our measurements indicate that the Ir NP is the most active one with a catalytic constant as high as  $6.27 \times 10^5 \text{ s}^{-1}$ , followed by Pt, Rh, and Pd NPs. The binding affinities of NPs to peroxidase substrates during catalysis were also quantitively analyzed and compared. Using enzyme-linked immunosorbent assay (ELISA) as a model biosensing platform, the performance of PGM NPs in detecting carcinoembryonic antigen (CEA, a cancer biomarker) was evaluated. The results showed that the detection sensitivity was correlated to the catalytic activity of PGM NPs, where Ir NPs achieved the highest sensitivity with a limit of detection at the level of low picogram per milliliter.

## **Table of Contents**



**Keywords:** Peroxidase · nanoparticle · controlled synthesis · catalysis · ELISA

#### INTRODUCTION

In the last decade or so, inorganic nanoparticles (NPs) of various materials have been reported to possess intrinsic peroxidase-like properties which can catalyze peroxide dependent redox reactions. 1-3 These NPs are commonly referred to as "peroxidase mimics". Notable examples of peroxides mimics include NPs made of carbons, metals, metal oxides, ceria, and a combination of them. 4-10 Compared to their natural counterparts (*e.g.*, horseradish peroxidase, HRP), peroxidase mimics are generally engineered to be more catalytically active. In addition, peroxidase mimics are non-protein materials and thus are more stable than natural peroxidases. These advantages of peroxidase mimics enable them to be a class of emerging materials for various biomedical applications such as biosensing, imaging, and therapy. 1,2

Among various types of peroxidase mimics, platinum-group metal (PGM) NPs have drawn particular attention owing to their unique features and outstanding performance in bio-applications, especially in *in vitro* diagnostics. For instance, PGM NPs possess higher catalytic activities than many other peroxidase mimics of the same dimensions. PGM NPs display excellent stabilities because they are made of inert noble metals. Moreover, the surfaces of PGM NPs can be conveniently functionalized with biomolecules through physical adsorption and/or metal-thiolate bonding. These features of PGM NPs make them particularly suitable for developing diagnostic techniques, such as those based on enzyme-linked immunosorbent assay (ELISA<sup>12,13</sup>) and lateral flow assay (LFA<sup>14,15</sup>) platforms. In a typical setup of a diagnostic system, PGM NPs are conjugated to bioreceptors (*e.g.*, antibodies and DNAs) and specifically generate colorimetric signal by catalyzing the oxidation of chromogenic substrates (*e.g.*, 3',3',5',5'-tetramethylbenzidine, TMB). A more active PGM NP is expected to produce a stronger signal at a lower analyte concentration, effectively enhancing the detection limit of the associated diagnostic system. As such, catalytic activity of a PGM NP is a critical parameter that largely determines its performance in diagnostic applications.

Over the last decade many newly designed PGM NPs have been produced which greatly enhance the catalytic constant ( $K_{\text{cat}}$ , a parameter that measures catalytic activity) of peroxidase mimics to record highs. <sup>17-20</sup> However significant, future progress towards enhanced PGM NPs-based diagnostic systems is severely hindered by an incomplete understanding of the peroxidase-like activity of this elemental class. Elucidating the activity of PGM NPs systematically gives researchers looking to study any peroxidase dependent processes the foundation for optimizing

sensing systems through ideal elemental selection.

In this work (see Figure 1 for a schematical diagram), we provide a benchmark trend for the peroxidase-like catalytic activity of four general PGM NPs, including those made of Pd, Pt, Rh and Ir, and describe their catalytic behavior in terms of traditional Michaelis-Menten kinetic parameters towards the oxidation of TMB by hydrogen peroxide. This trend is validated for diagnostic application using enzyme-linked immunosorbent assay (ELISA) of carcinoembryonic antigen (CEA, a cancer biomarker) as a model diagnostic system.<sup>21,22</sup>

## **EXPERIMENTAL SECTION**

Chemicals and abbreviations. All chemicals were sourced from the Sigma Aldrich Company unless otherwise noted. Palladium chloride 99% (PdCl<sub>2</sub>), Chloroplatinic acid hexahydrate 37.5% Pt basis (H2PtCl6• 6 H2O), Sodium hexachlororhodate hydrate (Na2RhCl6 • H2O), Sodium hexachloroiridate hydrate (Na<sub>2</sub>IrCl<sub>6</sub> • H<sub>2</sub>O), Hydrochloric acid 37% (HCl), Trisodium citrate dihydrate 99% (Na<sub>3</sub>C<sub>6</sub>H<sub>5</sub>O<sub>7</sub> • 2 H<sub>2</sub>O), Sodium borohydride 98% (NaBH<sub>4</sub>), Ethanol 95% (EtOH), Sodium acetate 99% (NaOAc), Acetic acid 99.7% (HOAc), 3',3',5',5'-tetramethylbenzidine 99% (TMB), Dimethyl sulfoxide 99.9% (DMSO), Hydrogen peroxide 10M (H<sub>2</sub>O<sub>2</sub>), Sodium bicarbonate 99.5-100% (NaHCO<sub>3</sub>), Sodium carbonate 99% (Na<sub>2</sub>CO<sub>3</sub>), Sodium phosphate monobasic 99% (Na<sub>2</sub>HPO<sub>4</sub>), Potassium phosphate dibasic 99% (KH<sub>2</sub>PO<sub>4</sub>), Potassium chloride 99% (KCl), Sodium chloride 99.5% (NaCl), Sodium azide 99.8% (N<sub>3</sub>Na), Bovine serum albumin 96%, Tween-20 polysorbate, Anti-CEA rabbit polyclonal antibody 0.5 mg mL<sup>-1</sup> (from Abcam), Anti-CEA mouse monoclonal antibody 0.5 mgmL<sup>-1</sup> (from Abcam), Goat anti-mouse IgG antibody 2.5 mg mL<sup>-1</sup> (from Invitrogen), HRP labeled goat anti-mouse IgG conjugate (Thermo Fisher Scientific, Inc.), Carcinoembryonic antigen 0.795 mgmL<sup>-1</sup> (from Millipore Sigma Company), Phosphate buffered saline (PBS) - 10.14 mM Na<sub>2</sub>HPO<sub>4</sub>, 1.76 mM KH<sub>2</sub>PO<sub>4</sub>, 2.68 mM KCl, 3.08 mM NaN<sub>3</sub>, 0.137 M NaCl, Phosphate buffered saline Tween (PBST) – PBS buffer with 0.05% v/v Tween-20 polysorbate, Carbonate buffer – 15.1 mM Na<sub>2</sub>CO<sub>3</sub>, 35 mM NaHCO<sub>3</sub>, 3.08 mM NaN<sub>3</sub>.

**Instrumentation.** All transmission electron microscopy (TEM) images, excluding insets, were taken using a JEOL-1011 transmission electron microscope. High resolution TEM images as insets were taken using an FEI Tecnai F30 TEM. Fourier transform-infrared spectroscopy (FT-IR) measurement were obtained using a Shimadzu IRSpirit Infrared Spectrometer. X-ray diffraction spectroscopy (XRD) analysis was performed using a PANalytical Empyrean X-Ray Diffractometer

utilizing a 1.8 KW Copper X-ray tube and spinning stage. All X-ray photoelectron spectroscopy (XPS) spectra were collected on a Physical Electronics 5400 ESCA X-Ray Photoelectron Spectrophotometer using a 300 µm spot and 0.100 eV step size. Inductively coupled plasma mass spectroscopy (ICP-MS) analysis was performed using a Thermo Scientific iCAP RQ. Dynamic light scattering (DLS) measurements were performed using a Zetasizer Nano ZS90, Malvern Panalytical. All UV-vis data for kinetic determination as well as scanning spectra were taken using an Agilent Cary 60 UV-vis spectrophotometer. UV-visible spectrum taken during ELISA were recorded using a BioTek Synergy H1 UV-vis microplate reader at 450 nm.

Synthesis of PGM Nanoparticles (NPs). All aqueous solutions, unless otherwise noted, were prepared using deionized (DI) water with a resistivity of 18.2 MΩ·cm. To synthesize Pd nanoparticles (Pd NPs) used for analysis seen in Figure 2, a 50 mL round bottom flask was filled with 38 mL of DI water. To this was added 1 mL of 46 mM trisodium citrate and 1 mL of 16 mM PdCl<sub>2</sub> dissolved in 32.4 mM HCl, which was placed to stir at room temperature for 10 minutes. After this time, 200 µL of a 0.1 M solution of NaBH<sub>4</sub> was freshly prepared and injected into the reaction flask drop by drop over 1 minute by pipette. A swift change in the color of solution from yellow to brown upon injection of the borohydride was observed and the reaction was allowed to progress for 30 minutes. Upon completion of the reaction at t = 30 minutes, the reaction contents were collected by ultracentrifugation at 186,000 RCF for 30 minutes to ensure complete separation of products. The particles were washed 3 times with DI water and suspended in DI water for further use. The syntheses to produce Pt NPs and Rh NPs shown in Figure 2 are identical to the synthesis for Pd NPs except for the substitution of the PdCl<sub>2</sub> + HCl precursor for (16 mM, 1 mL) H<sub>2</sub>PtCl<sub>6</sub> and (16 mM, 1 mL) Na<sub>2</sub>RhCl<sub>6</sub> respectively. To synthesize Ir NPs, a 100-mL round bottom flask was filled with 38 mL of DI water, 1 mL of 16 mM Na<sub>2</sub>IrCl<sub>6</sub>, 1 mL of 46 mM trisodium citrate and was heated to 55°C under bubbling N<sub>2</sub> gas with stirring for 30 minutes to remove dissolved O<sub>2</sub> gas. After bubbling, the N<sub>2</sub> gas was kept as a slow steady stream over the reaction contents to prevent the return of oxygen to the flask. Subsequently, 200 µL of 0.1 M NaBH<sub>4</sub> was freshly prepared and immediately injected into the reaction flask drop by drop over 1 minute by pipette. The reaction solution began turning grey after 2 minutes then changed to black after 10 minutes, indicating the formation of Ir NPs. The reaction was allowed to progress for a total of 30 minutes after NaBH<sub>4</sub> introduction and collected/ washed using the same protocol as other PGM NPs. 30% EtOH suspensions of PGM products were drop coated onto a Formvar/ carbon 200 mesh, copper TEM

grid for TEM analysis.

Kinetic Determination. Determination of the peroxidase activity of prepared PGM NPs was carried out by our previously published protocols with minor variation. <sup>17,18</sup> Measurements were taken within 3 hours of synthesis to ensure the freshness of the analyzed PGM NPs. 0.2 M NaOAc/HOAc, pH 4.0 was used as a pH buffer for reaction. 1.0 mL cuvette (path length, L=1.0 cm) was used to house the reaction within the spectrophotometer for analysis. Final particle concentrations used for kinetic analysis of PGM NPs are listed in Table 1. After addition of TMB and H<sub>2</sub>O<sub>2</sub> to a buffer solution containing the PGM NPs, the cuvette was promptly mixed by pipette and the absorbance of the reaction solution measured by UV-vis spectrophotometry at 653 nm using one read every 2 seconds for a total of 1 minute. Absorbance versus time curves were obtained to derive the linear slope at the beginning of reaction (Slope). The initial reaction velocity (v) was then calculated by the equation:

$$v = Slope/(\varepsilon_{TMB-653 nm} \cdot L)$$

where  $\epsilon_{TMB-653 \text{ nm}}$  is the molar extinction coefficient of oxidized TMB (oxTMB) at 653 nm (i.e.,  $3.9 \times 10^4 \text{ M}^{-1} \cdot \text{cm}^{-1})^{17}$  and L is the path length of the cuvette (1.0 cm). Then the plots of the initial velocity (v) against TMB concentrations were fitted using nonlinear regression of the Michaelis-Menten equation:

$$v = v_{\text{max}} \cdot [S]/(K_m + [S])$$

where  $K_m$  is the Michaelis constant,  $v_{max}$  is maximal reaction velocity, and [S] is either the concentration of TMB or  $H_2O_2$  dependent on the substrate being tested for. Kinetic parameters for TMB and  $H_2O_2$  substrates were obtained by measuring the rate of formation of oxTMB at 653 nm under different concentrations of substrate while maintaining all other factors constant. The average velocities of 3 individual trials were used to create Michaelis-Menten and double reciprocal plots. Kinetic parameters  $v_{max}$  and  $K_m$  were obtained using computer aided non-linear regression of the Michaelis-Menten curve using Origin software.

Preparation of the PGM NP-Goat Anti-mouse IgG Conjugates (PGM Conjugates). The ELISA assay was performed using protocols defined by our group's previous publications with minor modifications. <sup>17,23</sup> The PGM NPs-based ELISA begins with functionalization of the citrate coated PGM NPs through passive antibody conjugation. This was accomplished by first washing 2 mL of freshly prepared PGM NP reaction solution (as described in the Synthesis section) and dispersing into 500 μL of PBS buffer instead of DI water. In a 1.5 mL centrifuge tube, 50 μL of

this PGM NP suspension in PBS was mixed with 50  $\mu$ L of 2.5 mg mL<sup>-1</sup> goat anti-mouse IgG and was allowed to incubate at room temperature for 1 hour, after which was placed in a refrigerator overnight at 4°C. To block the PGM conjugates, to this suspension was added 100  $\mu$ L 5% w/v BSA in PBS and placed to gently shake for 2 hours. After this time the blocked PGM conjugates were collected by centrifugation, washed 3 times with PBS, and finally dispersed into 100  $\mu$ L 1% w/v BSA in PBS buffer for later use.

**PGM NPs-based ELISA of Carcinoembryonic Antigen (CEA)**.<sup>23</sup> 0.5 mg mL<sup>-1</sup> anti-CEA rabbit polyclonal antibody was diluted 100× in carbonate buffer, and 100 μL distributed to each well of a new 96-well microwell plate which was covered and stored at 4°C overnight. The next day, each well was washed 3 times using "washing buffer" (PBST) to remove residual unadhered antibody and 200 μL "blocking buffer" (2% w/v BSA in PBST) added to each well. The plate was covered, placed onto a mechanical shaker, and incubated at room temperature for 1 hour after which the wells were washed again with washing buffer 3 times.

Dilutions of CEA (~0.1 pg mL<sup>-1</sup> – 100 ng mL<sup>-1</sup>) in "dilution buffer" (1% w/v BSA in PBST) were prepared and 100  $\mu$ L of each added to their respective wells, with the first well (0 pg mL<sup>-1</sup>) being solely comprised of dilution buffer. The plate was covered, placed onto a shaker, incubated for 2 hours at room temperature, and subsequently washed 3 times with washing buffer. 2 mg mL<sup>-1</sup> anti-CEA mouse monoclonal antibody was diluted 1000× in dilution buffer and 100  $\mu$ L was added to each well. The plate was again covered, placed onto a shaker, incubated for 1 hour, and washed 3 times with washing buffer. To finish the PGM NPs-based ELISA a volume of PGM conjugates was diluted in dilution buffer (Pd 1:350, Pt 1:2000, Rh 1:450, Ir 1:3000) and 100  $\mu$ L was added to each well. The dilution factors of blocked PGM conjugates were determined in a separate ELISA performed beforehand, and the proper dilution of PGM conjugates was based on the amount necessary for the wells with 0 pg mL<sup>-1</sup> CEA to reach 0.15 – 0.17 absorbance units after an incubation time of 15 minutes. The microwell plate containing the blocked PGM conjugates was placed on a shaker, incubated for 1 hour, and washed 6 times with washing buffer.

Finally, 100  $\mu$ L of substrate solution composed of 0.8 mM TMB, 2 M H<sub>2</sub>O<sub>2</sub>, and 0.2 M pH 4 NaOAc/ HOAc buffer was injected into each well, placed on a shaker, and a timer immediately started thereafter. Wells with higher CEA concentrations begin to turn darker blue indicating the formation of oxTMB charge transfer complex ( $\lambda_{max}$  = 653 nm). After 15 minutes, 50  $\mu$ L of 2 M H<sub>2</sub>SO<sub>4</sub> was injected into each well to quench the reaction resulting in strongly yellow solutions,

indicative of conversion to the TMB diimine form ( $\lambda_{max} = 450$  nm). The plate was then analyzed on a UV-vis spectrophotometer at 450 nm. These absorbance values were used to plot absorbance versus CEA concentration and to determine the linear ranges in addition to limits of detection.

For the HRP-based ELISA, the procedure and the antibodies were kept the same as the PGM NPs-based ELISAs above, except for the substitution of PGM NP-goat anti-mouse IgG conjugates with HRP-goat anti-mouse IgG conjugates (1 µg/mL, in dilution buffer) and the change of substrate solution to 0.8 mM TMB and 5 mM H<sub>2</sub>O<sub>2</sub> in pH 5.0 citric acid/Na<sub>2</sub>HPO<sub>4</sub> buffer.

## **RESULTS AND DISCUSSION**

## **Synthesis and Characterizations**

It's known that the peroxidase-like activities of PGM NPs have strong dependence on their physicochemical parameters such as size, shape, and surface ligand. 11,24 Therefore, to meaningfully compare the peroxidase-like catalytic activity of prepared PGM NPs the only significant variable between materials should be elemental choice, while all other physicochemical parameters are kept the same or similar. In order to obtain PGM NPs that meet these criteria a sub-10 nm face-centered cubic (*fcc*) spherical morphology was selected on the basis that an *fcc* crystalline metals under thermodynamic control will first nucleate with a classic "Wulff shape" in order to minimize surface free energy. This could be accomplished by using a strong reducing agent (NaBH<sub>4</sub>) and dilute PGM precursor concentration to form many initial seeds which had limited potential to grow past 10 nm in size. Citrate was selected as an ideal capping agent due to its minimal impact on catalytic activity, as well as being an ideal surfactant for biomolecule conjugation. The synthetic method to produce PGM NPs used for analysis was carried out by modification of previously existing protocol for Pt NPs. and was successfully modified and applied to Pd, Rh, and Ir. Detailed synthetic procedures are provided in the Experimental Section above.

TEM images of as-synthesized PGM NPs are shown in Figure 2. Through careful computer aided measuring using ImageJ software, the particles' diameters were measured to be approximately 3.80, 3.72, 3.94, and 3.61 nm on average for Pd, Pt, Rh, and Ir NPs, respectively, with good uniformities. The average volume of the prepared PGM NPs was estimated by assuming a perfect spherical morphology and calculated using the average diameter obtained from TEM imaging. High-resolution TEM (HR-TEM) images of individual PGM NPs are shown as insets of

Figure 2. The HR-TEM images demonstrate {111} facet lattice spacing predominantly present on particle surfaces with no major defects. Additional TEM images of PGM NPs used for analysis can be found in Figure S1. Dynamic light scattering (DLS) measurements were performed to evaluate the dispersities of the four different PGM NPs in aqueous suspensions. As shown by Figure S2, only one narrow peak was observed for the size distribution of each NP, suggesting good monodispersity in size. It should be noted that the average hydrodynamic diameters of the NPs (7.15, 8.08, 6.26, and 7.15 nm for Pd, Pt, Rh, and Ir NPs, respectively) were larger than the average diameters measured from the TEM images. This differences can be ascribed to the solvation/chemical ligand layers on the NP surfaces, such as water and citrate molecules.

X-ray diffraction (XRD) analysis was invoked to gain a deeper understanding of the crystallinity of the materials. PGM NPs of each metal were sonicated with Vulcan XC-72 carbon for 1 hour to provide an inactive support for XRD measurements. Results in Figure 3a confirm the materials' *fcc* crystal structure is primarily composed of {111} facets and an equally proportional mixture of {200}, {220}, and {311} which agrees well with ICDD database records for the studied *fcc* PGM NPs. Note that the peaks of (222) planes are almost invisible in the XRD patterns due to the small sizes of NPs, which is consistent with previous reports. <sup>30,31</sup> Overall, the XRD data reveals good uniformity in surface facets between the four metals confirming the likeness in crystal structure.

Fourier transform infrared spectroscopy (FT-IR) analysis was performed to probe and confirm the presence of citrate ligand on the surface of the PGM NPs.<sup>32</sup> The resulting spectra of the carboxyl region can be found in Figure 3b and full spectral scans can be found in Figure S3. Peaks observed at 1400 and 1550 cm<sup>-1</sup> are representative of the carboxylate symmetric and asymmetric stretches respectively confirming the presence of citrate on the surface of the PGM NPs. Broad peaks between 3000-3300 cm<sup>-1</sup> in Figure S3 were attributed to be from the hydroxyl stretch, however the carboxylate peaks were most prominent. Note, these characteristic peaks of citrate absorbed on the NPs were consistent with the peaks from pristine citrate (Figure S4).

X-ray photoelectron spectroscopy (XPS) was employed to check the oxidation state of the prepared PGM NPs. XPS samples were prepared by drop coating freshly synthesized aqueous suspensions of PGMs onto a reflective silicon wafer which was dried and stored under N<sub>2</sub> gas until analyzed to preserve the surface oxidation environment of the PGM NPs. Resolved peaks shown in Figure 4 from scans of the 3d (Pd, Rh) and 4f (Ir, Pt) orbitals indicate that the PGMs are in their

native state primarily composed of zero valent PGM species with minimal surface oxidation. This was determined by computer aided multiple peak fitting of the C 1s charge corrected spectra. The primary peaks labeled in dark red and dark blue positioned at 335.3 (Pd 3d 5/2), 340.9 (Pd 3d 3/2), 71.0 (Pt 4f 7/2), 74.4 (Pt 4f 5/2), 307.4 (Rh 3d 5/2), 312.3 (Rh 3d 3/2), 61.1 (Ir 4f 7/2) and 64.1 eV (Ir 4f 5/2) are representative of PGM<sup>0</sup> species.<sup>33</sup> Lighter colored peaks (orange, purple, light brown, or light blue) contribute to higher energy signals associated with small amounts of oxidized surface atoms. Although there will always be some small amount of surface oxidation, it is important to note that the real-world application of these materials will also be impacted by the presence of dissolved oxygen during handling much the same way. In full spectral scans, carbon and oxygen peaks are observed, further hinting at the adherence of citrate to the surface of PGMs.

Taken together, these NPs, which have the same shape and capping agent on surface, similar sizes and surface areas, but different elemental compositions, could serve as an ideal platform to investigate the peroxidase-like activity of NPs of different PGMs and assess their performance in bio-applications.

# Peroxidase-Like Activity

The peroxidase oxidation product of TMB is a blue colored diimine charge transfer complex (oxTMB complex) with absorption maximum at 653 nm. 34,35 Traditionally, horseradish peroxidase (HRP) has been used as a benchmark enzyme to measure the catalytic activity of peroxidase mimics as it is one of the most commonly utilized, naturally occurring peroxidases. A schematic of the PGM NPs catalyzed TMB peroxidase reaction can be seen in Figure 5a. Absorbance spectra in Figure 5b shows the typical plot observed for the standard kinetic solution (blue cuvette) and the standard kinetic solution without PGM NPs (clear cuvette). This validates the PGM NP's critical role in catalyzing the oxidation of TMB by H<sub>2</sub>O<sub>2</sub>. It should be pointed out that the PGM NPs are expected to be oxidized (to some extent) by oxygen from the air and/or solution. 36 As such, the surfaces of NPs will be partially covered by metal oxides as a function time which may influence the catalytic efficiency. As shown by the results in Figure S5, the catalytic activities of all four types of PGM NPs were reduced after they had been stored in water for 10 months. To rule out the factor of metal oxidation, we used freshly prepared NPs for comparison in this study.

Peroxidase-like catalytic properties of each PGM NP were independently evaluated by traditional Michaelis-Menten analysis using the oxidation reaction of TMB by H<sub>2</sub>O<sub>2</sub>. <sup>18,19</sup> The ideal

conditions for this reaction were selected to be pH 4, 2 M  $H_2O_2$ , 0.8 mM TMB, and a dilution of PGM catalyst, based on our previous publications. These parameters were collected by measuring the progression of absorbance at 653 nm of the kinetic solution while varying the concentrations of substrates TMB and  $H_2O_2$  in separate trials. These plots along with reciprocal "Lineweaver-Burke" plot insets can be found in Figure 6, where each data point is representative of three independent trials. Computer aided fitting of the Michaelis-Menten curve using Origin software was used to obtain the maximum velocity of reaction ( $\nu_{max}$ ) and the Michaelis constant ( $\kappa_{m}$ ) by the equation (1) shown in Figure S6 and subsequent reciprocal plots by equation (2) in Figure S6.

It is known that some nanomaterials of PGMs, especially Rh, are not fully soluble in aquaregia even at elevated temperatures and therefore inductively coupled plasma mass spectroscopy (ICP-MS) was ruled out as a viable option to precisely determine the molar concentration of PGM NPs used in the kinetic solution.<sup>38</sup> To circumvent this issue the volume of PGM NPs within the cuvette was determined by each metals' density and the mass of PGM in the precursors used during synthesis considering the dilution factors necessary to perform kinetic experiments. A molar excess of strong reducing agent (NaBH4) and careful collection by ultracentrifugation was used to ensure negligible loss of nanoparticles during synthesis. The produced PGMs are spherical in nature and as such their average volumes were calculated by equation (3) in Figure S6. Other equations used to determine the molar concentrations of PGM NPs in the kinetic solutions as well as kinetic parameters can be found in Figure S6. Since particle concentration of Pd NPs has been commonly quantified using ICP-MS,<sup>39</sup> we used it as a benchmark to validate the quantification method illustrated in Figure S6. It turned out that the concentrations of Pd NPs in kinetic solution obtained from ICP-MS measurement and the method in Figure S6 were close (2.11 ×10<sup>-10</sup> versus 2.28 ×10<sup>-10</sup> M).

Results of the kinetic determination for TMB substrate are summarized in Table 1, where Michaelis-Menten graphs and results for  $H_2O_2$  substrate can be found in Figure S7 and Table S1, respectively. All PGMs were found to rapidly catalyze the oxidation of TMB, generating colored products (*i.e.*, oxTMB). The catalytic constant ( $K_{cat}$ , which is defined as the maximum number of products generated per second per catalyst) as a key parameter measures the catalytic efficiency.  $^{17,18,40}$  Of the PGM NPs studied the  $K_{cat}$  values towards TMB ranged from  $4.79 \times 10^4$  to  $6.27 \times 10^5$  s<sup>-1</sup> with Ir NPs being the most active ( $K_{cat} = 6.27 \times 10^5$  s<sup>-1</sup>) followed by Pt NPs ( $K_{cat} = 6.27 \times 10^5$  s<sup>-1</sup>) followed by Pt NPs ( $K_{cat} = 6.27 \times 10^5$  s<sup>-1</sup>)

 $2.38\times10^5~{\rm s}^{-1}$ ), Rh NPs (K<sub>cat</sub> =  $6.40\times10^4~{\rm s}^{-1}$ ), and lastly Pd NPs (K<sub>cat</sub> =  $4.79\times10^4~{\rm s}^{-1}$ ) (see Table 1). Using HRP as a model peroxidase, K<sub>cat</sub> values were enhanced by approximately 12, 16, 60, and 157 times respectively.<sup>4</sup> Notably, Pd NPs showed the lowest K<sub>m</sub> ( $5.64\times10^{-5}~{\rm M}$ ) suggesting that it binds the tightest to TMB substrate followed by Pt NPs (K<sub>m</sub> =  $1.60\times10^{-4}~{\rm M}$ ), Ir NPs (K<sub>m</sub> =  $2.50\times10^{-4}~{\rm M}$ ), and weakest to Rh NPs (K<sub>m</sub> =  $4.34\times10^{-4}~{\rm M}$ ).

While the explicit mechanisms of metallic NPs-catalyzed oxidation of TMB by H<sub>2</sub>O<sub>2</sub> has not been fully understood as of today, recent studies have demonstrated that the generation of hydroxyl radicals (•OH) from decomposition of H<sub>2</sub>O<sub>2</sub> and the oxidation of TMB by •OH are the key steps of this catalytic reaction. <sup>18,41</sup> To understand why Ir NPs among other PGM NPs show the highest catalytic activity, in a set of experiments we have determined and compared the efficiencies of different PGM NPs in generating •OH from H<sub>2</sub>O<sub>2</sub> using terephthalic acid as a fluorescent probe. <sup>17</sup> As shown by Figure S8, Ir NP is the most active one in generating •OH, which may be responsible for their superior catalytic efficiency towards oxidation of TMB by H<sub>2</sub>O<sub>2</sub> relative to other types of PGM NPs. More in-depth comparisons and simulation work are the subject of our future research.

# Performance in ELISA platform

To compare the performance of PGM NPs in biosensing, ELISA is chosen as a model diagnostic platform and carcinoembryonic antigen (CEA) as a model disease biomarker is detected. The principle of PGM NPs-based ELISA of CEA is shown in Figure 7a. <sup>21,23</sup> Specifically, the assay was performed in a 96-well microwell plate where rabbit-anti CEA polyclonal antibodies capable of trapping CEA were incubated. Addition of CEA thereafter allows for binding to rabbit antibodies and further incubation with mouse anti-CEA monoclonal antibodies effectively immobilizes CEA to the microwell plate. Thereafter, PGM NP-goat anti-mouse IgG conjugates were added to specifically generate color signal for detection and quantification. It is worthwhile noting that the average numbers of antibodies on the four types of PGM NPs were estimated to be very close (*i.e.*, in the range of 1.53-1.66 per NP, see detailed data in Table S2) as determined by measurement of antibody absorption at OD<sub>280 nm</sub>. <sup>42,43</sup> In addition, the catalytic activities of all the four types of PGM NPs remained almost unchanged after antibody conjugation (see Figure S9), which might be ascribed to the fact that H<sub>2</sub>O<sub>2</sub> and TMB are much smaller than goat-anti mouse IgG molecule and thus they can still effectively access to NP surface during catalysis. Detailed ELISA procedure is provided in the Experimental Section above.

A photo of a typical analyzed microwell plate and results of the ELISA assay can be found in Figure 7b,c. Each data point is representative of the average of four trials per PGM NP. As expected, PGM NPs were able to detect CEA antigen at monumentally different concentrations. Ir NP was able to reach the lowest limit of detection (LOD), determined by the 3 times standard deviation method,<sup>44</sup> (11.3 pg mL<sup>-1</sup>). This was followed by Pt NPs (LOD = 36.3 pg mL<sup>-1</sup>), Rh NPs (LOD = 154.1 pg mL<sup>-1</sup>), and lastly Pd NPs (LOD = 740.1 pg mL<sup>-1</sup>). The trend of detection sensitivity is in good agreement with the catalytic efficiencies (K<sub>cat</sub>) of PGM NPs towards TMB as determined by the kinetic assay (Table 1). Such a correlation can be understood from the assumption that a PGM NP with a greater K<sub>cat</sub> towards TMB is expected to produce a stronger colorimetric signal (arising from oxidized TMB) at a lower analyte concentration, enhancing the sensitivity of ELISA. In comparison, the LOD of HRP-based ELISA of CEA that was assembled using the same set of antibodies was determined to be approximately 1620 pg/mL based on its calibration curve (Figure S10).

The linear ranges (insets of Figure 7c) were determined to be 1,000-25,000 pg mL<sup>-1</sup> (Pd NPs), 500-75,000 pg mL<sup>-1</sup> (Pt NPs), 1,000-50,000 pg mL<sup>-1</sup> (Rh NPs), and 500-75,000 pg mL<sup>-1</sup> (Ir NPs). The slopes of the linear ranges are a function of the change in signal intensity per pg mL<sup>-1</sup> increase in CEA concentration and therefore a larger slope suggests higher efficiency for biosensing. The slopes obtained from the linear ranges were 0.075, 0.195, 0.138, and 0.284 for Pd, Pt, Rh, and Ir NPs respectively with good correlations. A table summarizing the analytical performance of different PGM NPs-based ELISAs is provided in the Supporting Information (see Table S3).

## **CONCLUSION**

In summary, this work systematically investigated and compared the peroxidase-like catalytic properties of four common PGM NPs made of Pd, Pt, Rh, and Ir. These NPs were carefully analyzed and determined to all possess FCC crystal structure, citrate as a stabilizing surfactant, predominantly zero valent oxidation states, and sizes in the range of 3.61-3.94 nm. Due to the unique similarity of the designed nanomaterials the differences in catalytic properties can be primarily ascribed to the impact of elemental composition. Among these PGM NPs, Ir NPs were found to be the most catalytically active, which possess a catalytic constant (K<sub>cat</sub>) as high as 6.27×10<sup>5</sup> s<sup>-1</sup>. Pt NPs were the second most active, followed by Rh NP and Pd NP as the two less active PGM NPs. This trend in catalytic activity was consistent with their performance in ELISA

of protein biomarkers, finding Ir NPs could reach the highest detection sensitivity with a LOD at

the level of low pg mL<sup>-1</sup> followed expectedly by Pt, Rh, and lastly Pd NPs. The findings in this

study may inspire new research directions in the field of enzyme mimic development critical to

the advancement of applied nanomaterials for biosensing.

ASSOCIATED CONTENT

**Supporting Information** 

Additional images, plots, spectra, and tables. The Supporting Information is available free of

charge on the ACS Publications website.

**AUTHOR INFORMATION** 

**Corresponding Author** 

\*E-mail: Xiaohu.Xia@ucf.edu

**Notes** 

The authors declare no competing financial interests.

**ACKNOWLEDGEMENTS** 

This work was supported in part by the grants from the National Science Foundation (CBET-

1804525 and CHE-1834874), the National Institute of Food and Agriculture, U.S. Department of

Agriculture (2020-67021-31257), and the startup funds from University of Central Florida (UCF).

14

#### REFERENCES

- 1. Ye, H.; Xi, Z.; Magloire, K.; Xia, X. Noble-metal nanostructures as highly efficient peroxidase mimics. *ChemNanoMat* **2019**, *5*, 860-868.
- 2. Wu, J.; Wang, X.; Wang, Q.; Lou, Z.; Li, S.; Zhu, Y.; Qin, L.; Wei, H. Nanomaterials with enzyme-like characteristics (nanozymes): Next-generation artificial enzymes (II). *Chem. Soc. Rev.* **2019**, *48*, 1004-1076.
- 3. Wang, H.; Wan, K.; Shi, X. Recent advances in nanozyme research. *Adv. Mater.* **2019**, *31*, 1805368.
- 4. Gao, L.; Zhuang, J.; Nie, L.; Zhang, J.; Zhang, Y.; Gu, N.; Wang, T.; Feng, J.; Yang, D.; Perrett, S. Intrinsic peroxidase-like activity of ferromagnetic nanoparticles. *Nat. Nanotechnol.* **2007**, *2*, 577-583.
- 5. Niu, L.; Cai, Y.; Dong, T.; Zhang Y.; Liu, X.; Zhang, X.; Zeng, L.; Liu, A. Vanadium nitride@carbon nanofiber composite: Synthesis, cascade enzyme mimics and its sensitive and selective colorimetric sensing of superoxide anion. *Biosens. Bioelectron.* **2022**, *210*, 114285.
- 6. Song, Y.; Qu, K.; Zhao, C.; Ren, J.; Qu, X. Graphene oxide: Intrinsic peroxidase catalytic activity and its application to glucose detection. *Adv. Mater.* **2010**, *22*, 2206-2210.
- 7. Cai, Y.; Liu, A. Heirarchical porous MoS<sub>2</sub> particles: excellent multi-enzyme-like activities, mechanism and its sensitive phenol sensing based on inhibition of sulfite oxidase mimics. *J. Hazard. Mater.* **2022**, *425*, 128053.
- 8. He, W.; Wu, X.; Liu, J.; Hu, X.; Zhang, K.; Hou, S.; Zhou, W.; Xie, S. Design of AgM bimetallic alloy nanostructures (M = Au, Pd, Pt) with tunable morphology and peroxidase-like activity. *Chem. Mater.* **2010**, *22*, 2988-2994.
- André, R.; Natálio, F.; Humanes, M.; Leppin, J.; Heinze, K.; Wever, R.; Schröder, H.-C.;
  Müller, W.; Tremel, W. V<sub>2</sub>O<sub>5</sub> nanowires with an intrinsic peroxidase-like activity. *Adv. Funct. Mater.* 2010, 21, 501-509.
- 10. Yan, L.; Mu, J.; Ma, P.; Li, Q.; Yin, P.; Liu, X.; Cai, Y.; Yu, H.; Liu, J.; Wang, G.; Liu, A. Gold nanoplates with superb photothermal efficiency and peroxidase-like activity for rapid and synergistic antibacterial therapy. *Chem. Commun.* **2021**, *57*, 1133-1136.
- 11. Wei, Z.; Xi, Z.; Vlasov, S.; Ayala, J.; Xia, X. Nanocrystals of platinum-group metals as peroxidase mimics for in vitro diagnostics. *Chem. Commun.* **2020**, *56*, 14962-14975.
- 12. Gao, Y.; Zhou, Y.; Chandrawati R. Metal and metal oxide nanoparticles to enhance the

- performance of enzyme-linked immunosorbent assay (ELISA). *ACS Appl. Nano Mater.* **2019**, *3*, 1-21.
- Damborska, D.; Bertok, T.; Dosekova, E.; Holazova, A.; Lorencova, L.; Kasak, P.; Tkac, J. Nanomaterial-based biosensors for detection of prostate specific antigen. *Microchimica Acta* 2017, 184, 3049-3067.
- 14. Ye, H.; Xia, X. Enhancing the sensitivity of colorimetric lateral flow assay (CLFA) through signal amplification techniques. *J. Mater. Chem. B* **2018**, *6*, 7102-7111.
- 15. Mulvaney, S. P.; Kidwell, D. A.; Lanese, J. N.; Lopez, R. P.; Sumera, M. E.; Wei, E. Catalytic lateral flow immunoassays (cLFIA<sup>TM</sup>): Amplified signal in a self-contained assay format. *Sens. Bio-Sens. Res.* **2020**, *30*, 100390.
- 16. Tao, X.; Wang, X.; Liu, B.; Liu, J. Conjugation of antibodies and aptamers on nanozymes for developing biosensors. *Biosens. Bioelectron.* **2020**, *168*, 112537.
- 17. Xia, X.; Zhang, J.; Lu, N.; Kim, M. J.; Ghale, K.; Xu, Y.; McKenzie, E.; Liu, J.; Ye, H. Pd–Ir core–shell nanocubes: a type of highly efficient and versatile peroxidase mimic. *ACS Nano* **2015**, *9*, 9994-10004.
- 18. Xi, Z.; Wei, K.; Wang, Q.; Kim, M. J.; Sun, S.; Fung, V.; Xia, X. Nickel-Platinum Nanoparticles as Peroxidase Mimics with a Record High Catalytic Efficiency. *J. Am. Chem. Soc.* **2021**, *143*, 2660-2664.
- 19. Xi, Z.; Cheng, X.; Gao, Z.; Wang, M.; Cai, T.; Muzzio, M.; Davidson, E.; Chen, O.; Jung, Y.; Sun, S. Strain effect in palladium nanostructures as nanozymes. *Nano Lett.* **2019**, *20*, 272-277.
- 20. Chen, G.; Qin, Y.; Jiao, L.; Huang, J.; Wu, Y.; Hu, L.; Gu, W.; Xu, D.; Zhu, C. Nanozyme-activated synergistic amplification for ultrasensitive photoelectrochemical immunoassay. *Anal. Chem.* **2021**, *93*, 6881-6888.
- 21. Lequin, R. M., Enzyme immunoassay (EIA)/enzyme-linked immunosorbent assay (ELISA). *Clin. Chem.* **2005**, *51*, 2415-2418.
- 22. Reen, D. J. *Basic Protein and Peptide Protocols*, Vol. 32.; Enzyme-linked immunosorbent assay (ELISA). **1994**, 461-466. https://doi.org/10.1385/0-89603-268-X:461
- 23. Xi, Z.; Gao, W.; Xia, X. Size Effect in Pd-Ir Core-Shell Nanoparticles as Nanozymes. *ChemBioChem* **2020**, *21*, 2440-2444.
- 24. Dai, Y.; Wang, Y.; Liu, B.; Yang, Y. Metallic nanocatalysis: an accelerating seamless integration with nanotechnology. *Small* **2015**, *11*, 268-289.

- 25. Wu, Z.; Yang, S.; Wu, W. Shape control of inorganic nanoparticles from solution. *Nanoscale* **2016**, *8*, 1237-1259.
- 26. Thanh, N. T.; Maclean, N.; Mahiddine, S. Mechanisms of nucleation and growth of nanoparticles in solution. *Chem. Rev.* **2014**, *114*, 7610-7630.
- 27. Hu, J.; Mi, H.; Wang, N.; Zhu, H.; Guo, W.; Zhang, S.; Shi, F.; Lei, Z.; Liu, Z.-H.; Jiang, R. Tuning the catalytic activity of colloidal noble metal nanocrystals by using differently charged surfactants. *Nanoscale* **2018**, *10*, 5607-5616.
- 28. Jazayeri, M. H.; Amani, H.; Pourfatollah, A. A.; Pazoki-Toroudi, H.; Sedighimoghaddam, B., Various methods of gold nanoparticles (GNPs) conjugation to antibodies. *Sens. Bio-Sens. Res.* **2016**, *9*, 17-22.
- 29. Wu, G.-W.; He, S.-B.; Peng, H.-P.; Deng, H.-H.; Liu, A.-L.; Lin, X.-H.; Xia, X.-H.; Chen, W. Citrate-capped platinum nanoparticle as a smart probe for ultrasensitive mercury sensing. *Anal. Chem.* **2014**, *86*, 10955-10960.
- 30. Wang, Y.; Biby, A.; Xi, Z.; Liu, B.; Rao, Q.; Xia, X. One-pot synthesis of single-crystal palladium nanoparticles with controllable sizes for applications in catalysis and biomedicine. *ACS Appl. Nano. Mater.* **2019**, *2*, 4605-4612.
- 31. Islam, M.; Rosales, J.; Saenz-Arana, R.; Ghadimi, S.; Noveron, J. Rapid synthesis of ultrasmall platinum nanoparticles supported on microporous cellulose fibers for catalysis. *Nanoscale Adv.* **2019**, *1*, 2953-2964
- 32. Xi, Z.; Gao, W.; Biby, A.; Floyd, A.; Xia, X. Ultrasmall Iridium Nanoparticles as Efficient Peroxidase Mimics for Colorimetric Bioassays. *ACS Appl. Nano Mater.* **2022**, *5*, 6089-6093.
- 33. NIST X-ray Photoelectron Spectroscopy Database, NIST Standard Reference Database Number 20, National Institute of Standards and Technology, Gaithersburg MD, 20899 (2000). https://srdata.nist.gov/xps/ (Accessed on 02 February 2022).
- 34. Josephy, P. D.; Eling, T. E.; Mason, R. P. The Horseradish Peroxidase-Catalyzed Oxidation of 3,5,3',5' Tetramethylbenzidine. Free Radical and Charge-Transfer Complex Intermediates. *J. Biol. Chem.* **1982**, *257*, 3669-3675.
- 35. Attar, F.; Shahpar, M. G.; Rasti, B.; Sharifi, M.; Saboury, A. A.; Rezayat, S. M.; Falahati, M. Nanozymes with intrinsic peroxidase-like activities. *J. Mol. Liq.* **2019**, *278*, 130-144.
- 36. Long, R.; Zhou, S.; Wiley, B.; Xiong, Y. Oxidative etching for controlled synthesis of metal nanocrystals: atomic addition and subtraction. *Chem. Soc. Rev.* **2014**, *43*, 6288-6310.

- 37. Davidson, E.; Xi, Z.; Gao, Z.; Xia, X. Ultrafast and sensitive colorimetric detection of ascorbic acid with Pd-Pt core-shell nanostructure as peroxidase mimic. *Sensors International* **2020**, *1*, 100031.
- 38. Forte, F.; Riano, S.; Binnemans, K. Dissolution of noble metals in highly concentrated acidic salt solutions. *Chem. Commun.* **2020**, *56*, 8230-8232.
- 39. Xie, S.; Choi, S.; Lu, N.; Roling, L.; Herron, J.; Zhang, L.; Park, J.; Wang, J.; Kim, M.; Xie, Z.; Mavrikakis, M.; Xia, Y. Atomic layer-by-layer deposition of Pt on Pd Nanocubes for catalysts with enhanced activity and durability toward oxygen reduction. *Nano Lett.* **2014**, *14*, 3570-3576.
- 40. Wu, Y.; Song, M.; Xin, Z.; Zhang, X.; Zhang, Y.; Wang, C.; Li, S.; Gu, N. Ultra-small particles of iron oxide as peroxidase for immunohistochemical detection. *Nanotechnology* **2011**, *22*, 225703.
- 41. Ge, C.; Fang, G.; Shen, X.; Chong, Y.; Wamer, W.; Gao, X.; Chai, Z.; Chen, C.; Yin, J. Facet energy versus enzyme-like activities: The unexpected protection of palladium nanocrystals against oxidative damage. *ACS Nano.* **2016**, *10*, 10436-10445.
- 42. Dawes, C.; Jewess, P.; Murray, D. Thiophilic paramagnetic particles as a batch separation medium for the purification of antibodies from various source materials. *Anal. Biochem.* **2005**, *338*, 186-191.
- 43. East, D.; Mulvihill, D.; Todd, M.; Bruce, I. QD-antibody conjugates via carbodiimide-mediated coupling: A detailed study of the variables involved and a possible new mechanism for the coupling reaction under basic aqueous conditions. *Langmuir* **2011**, *27*, 13888-13896.
- 44. Armbruster, D. A.; Tillman, M. D.; Hubbs, L. M. Limit of detection (LQD)/limit of quantitation (LOQ): comparison of the empirical and the statistical methods exemplified with GC-MS assays of abused drugs. *Clin. Chem.* **1994**, *40*, 1233-1238.

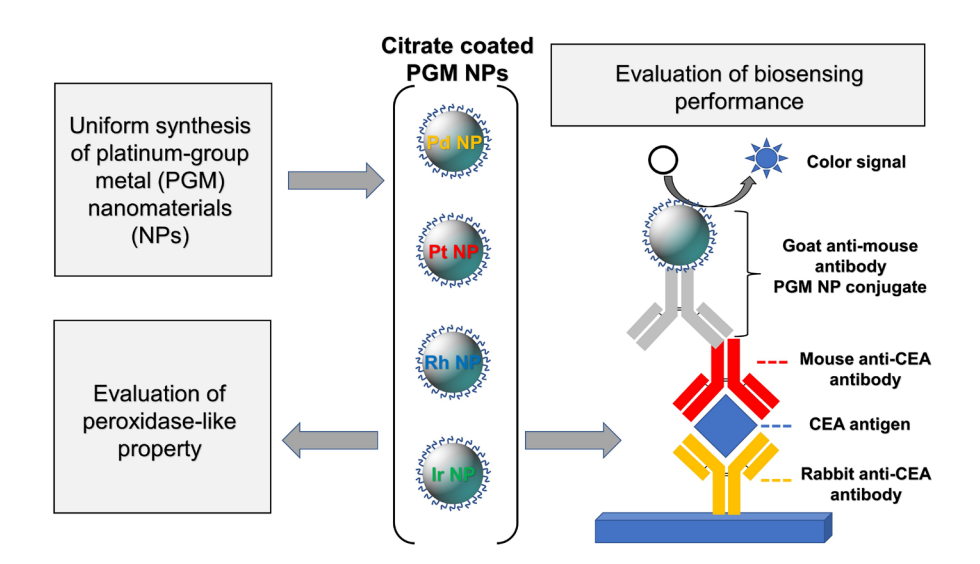


**Figure 1.** Schematical representation of the studied system where nanoparticles made of Pd, Pt, Rh, and Ir are systematically evaluated for their peroxidase-like properties and performance in a typical colorimetric biosensing platform.

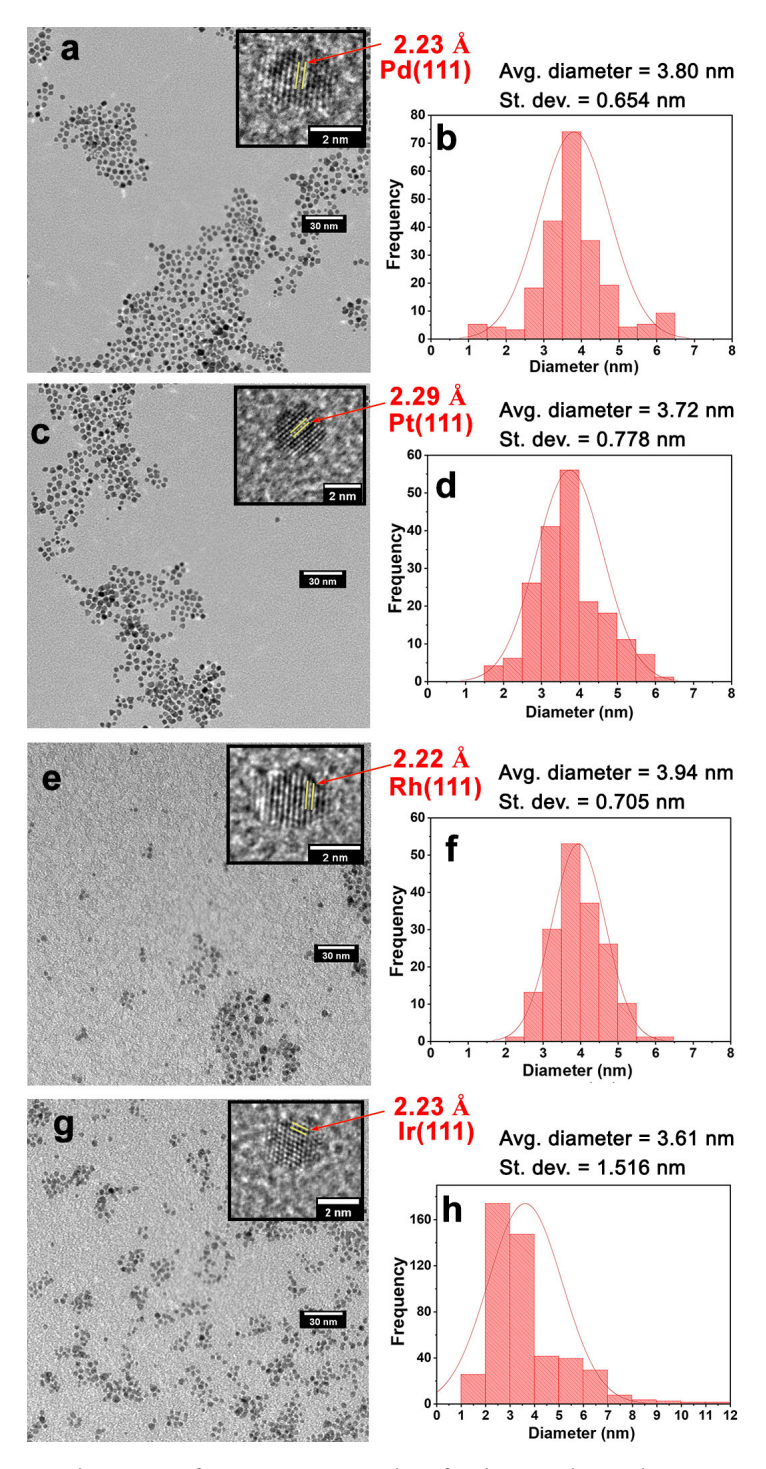


**Figure 2.** (a,c,e,g) TEM images of PGM NPs made of Pd, Pt, Rh, and Ir, respectively. Insets show high-resolution TEM images of individual NPs; (b,d,f,h) Corresponding size distribution charts of the PGM NPs.

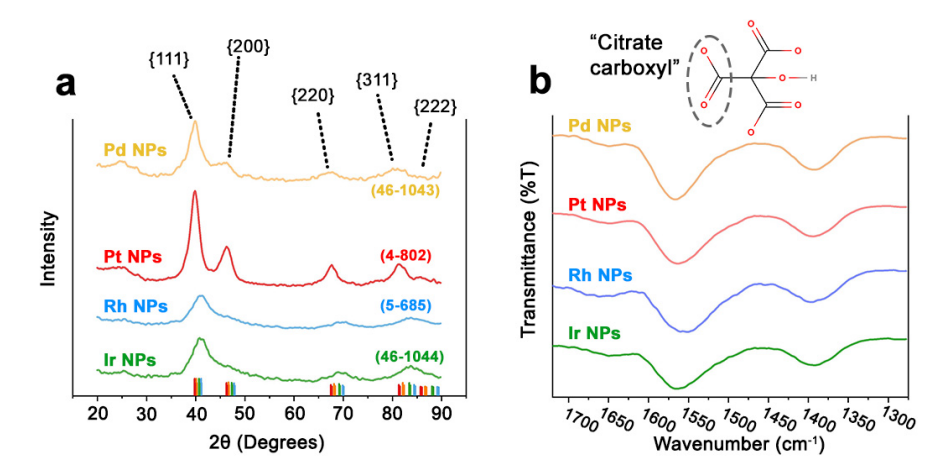


**Figure 3. (a)** XRD patterns recorded from different PGM NPs shown in Figure 1. The numbers in parenthesis signify the ICDD entry number from which peak locations are represented as vertical lines on the x-axis; **(b)** FT-IR spectra recorded from the PGM NPs. Full FT-IR scans are provided in Figure S3.

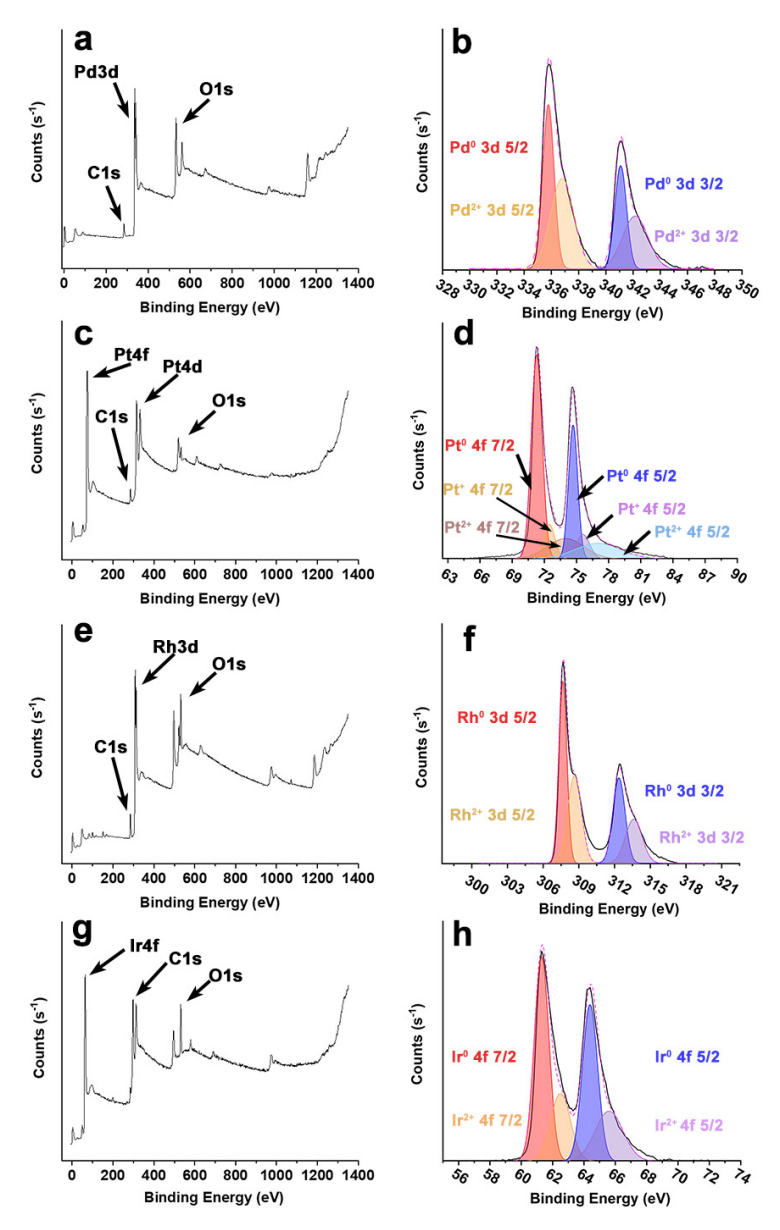


**Figure 4.** (a,c,e,g) Full XPS spectral surveys of the PGM NPs made of Pd, Pt, Rh, and Ir, respectively; (b,d,f,h) Individual scans of the Pd3d, Pt4f, Rh3d, and Ir4f orbitals. Darkest red and blue peaks represent signals from zero valent species where orange, pink, and light blue colored peaks indicate the presence of oxidixed PGM species.

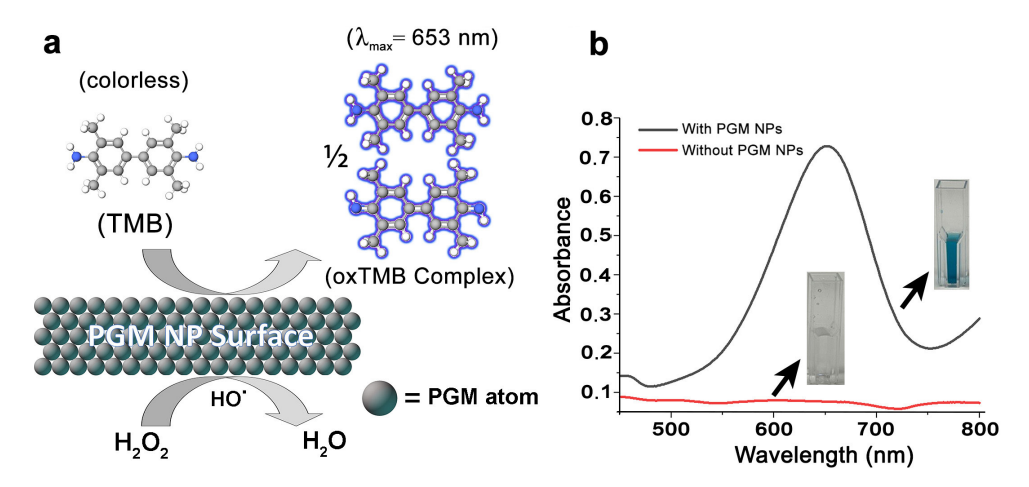


**Figure 5. (a)** Schematical representation of the TMB peroxidase reaction on the surface of a PGM NP catalyst to produce the blue colored TMB-diimine charge transfer complex (oxTMB) with absorbance maximum = 653 nm. **(b)** UV-vis spectra of the TMB peroxidase reaction kinetic solutions in the presence of (blue) and absence of (clear) PGM NPs demonstrating the role of PGM NPs as catalysts. The reaction kinetic solution consists of 2 M H<sub>2</sub>O<sub>2</sub> and 0.8 mM TMB in sodium acetate/acetic acid (NaOAc/HOAc) buffer solution pH 4.0.

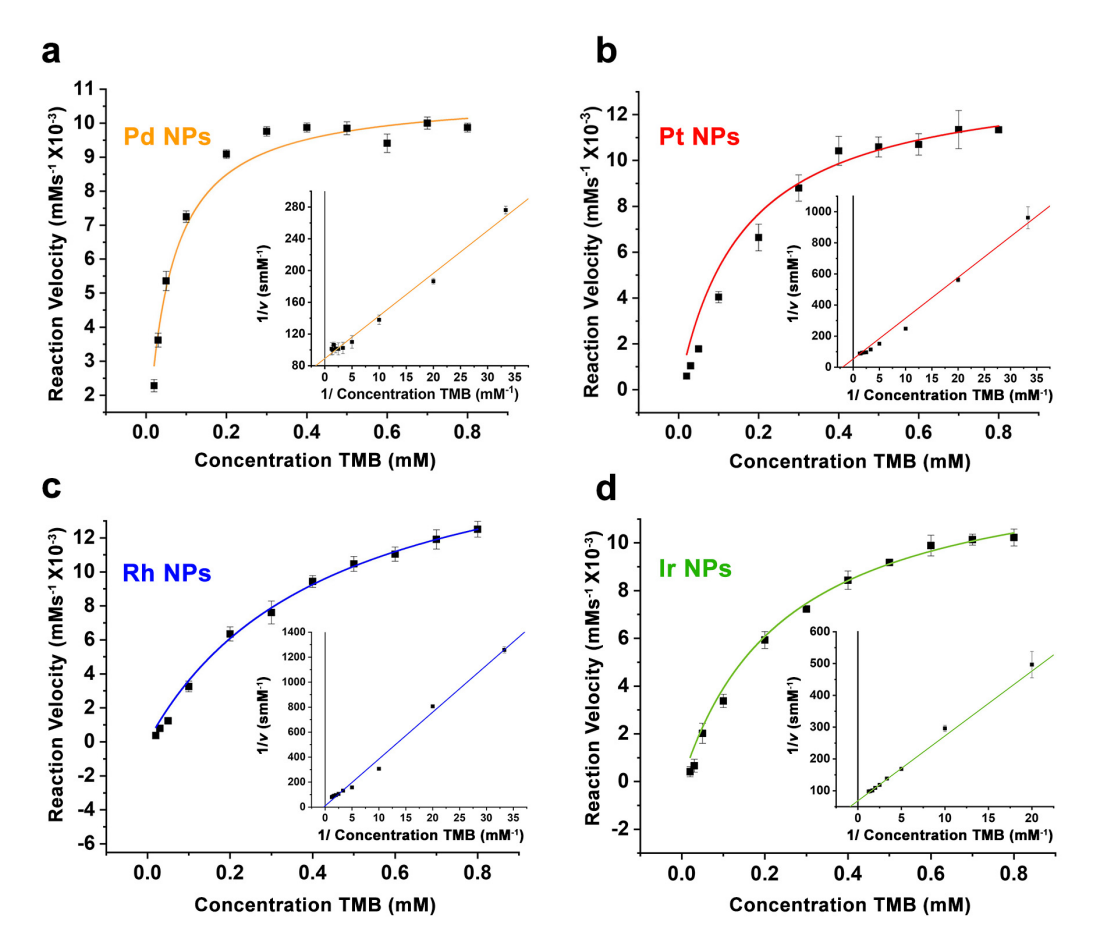


**Figure 6.** Results of kinetic assays for PGM NPs made of Pd (a), Pt (b), Rh (c), and Ir (d) towards TMB substrate plotted as reaction velocity (v) *versus* concentration of TMB (mM). Corresponding double reciprocal plots are shown in insets. Error bars indicate standard deviations of three independent measurements.

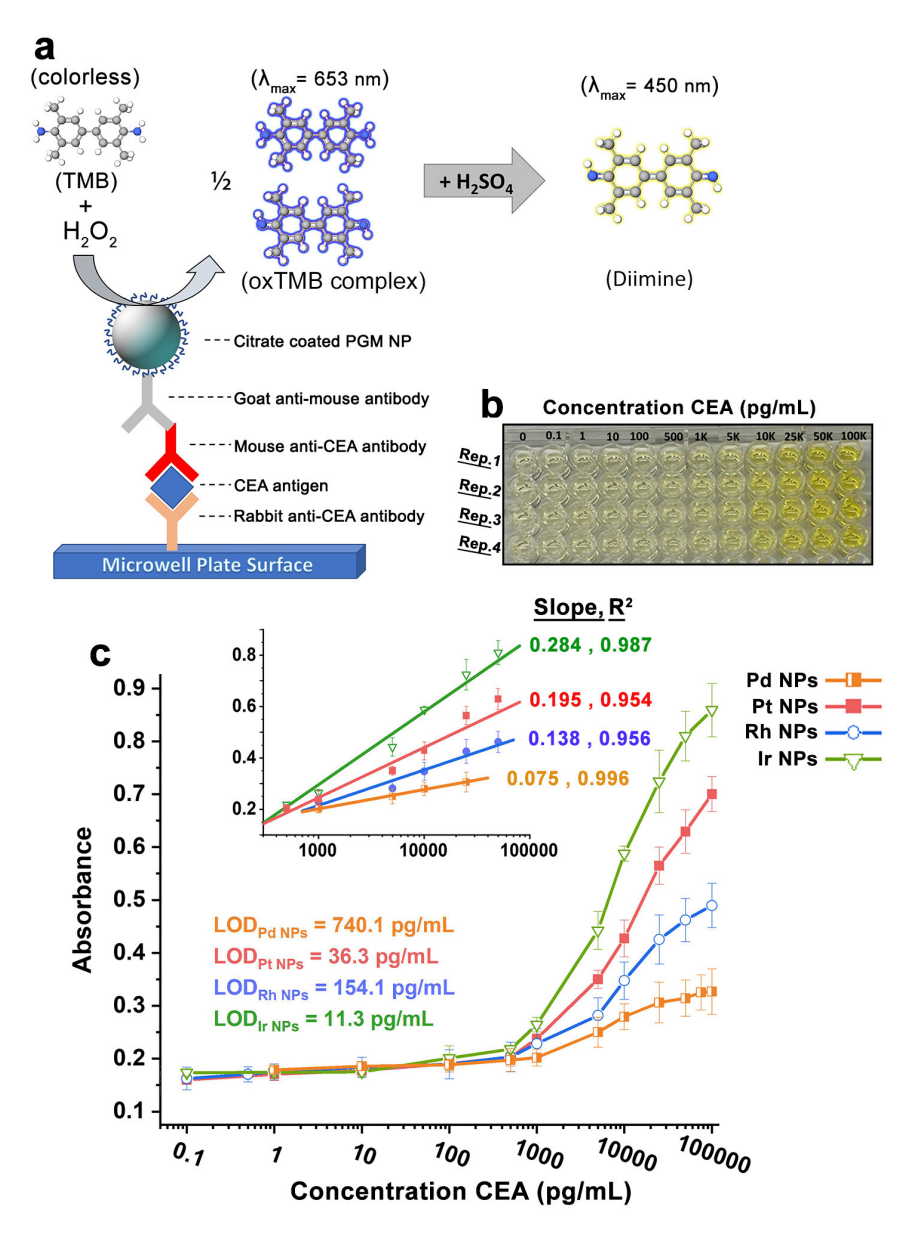


**Figure 7. (a)** Schematics of the PGM NPs-based ELISA of CEA; **(b)** Representative photographs taken from Ir NP-based ELISA of CEA standards. Each row represents an individual trial with CEA concentrations in units of pg/mL; **(c)** calibration curves along with linear range regions (inset) of the ELISAs of CEA. Error bars indicate standard deviations of four independent measurements.

**Table 1.** Comparison of the kinetic parameters of different PGM NPs toward substrate TMB. [E] represents the molar PGM NP concentration,  $K_m$  is the Michaelis constant,  $v_{max}$  is the maximal reaction velocity, and  $K_{cat}$  is the catalytic constant that equals to  $v_{max}/[E]$ .

Particle conditions			Kinetic parameters toward TMB		
catalyst	diameter (nm)	[E] (M)	$K_m(M)$	$v_{\text{max}} (\text{Ms}^{-1})$	Kcat (s <sup>-1</sup> )
Pd NPs	3.80	$2.28 \times 10^{-10}$	$5.64 \times 10^{-5}$	$1.09 \times 10^{-5}$	$4.79 \times 10^4$
Pt NPs	3.72	$5.81 \times 10^{-11}$	$1.60 \times 10^{-4}$	$1.38 \times 10^{-5}$	$2.38 \times 10^{5}$
Rh NPs	3.94	$3.02 \times 10^{-10}$	$4.34 \times 10^{-4}$	$1.93 \times 10^{-5}$	$6.40 \times 10^4$
Ir NPs	3.61	$2.19 \times 10^{-11}$	$2.50 \times 10^{-4}$	$1.37 \times 10^{-5}$	$6.27 \times 10^5$